nature biomedical engineering

ARTICLES

https://doi.org/10.1038/s41551-021-00809-7

Check for updates

Quantitative imaging of apoptosis following oncolytic virotherapy by magnetic resonance fingerprinting aided by deep learning

Or Perlman[1]✉, Hirotaka Ito[2], Kai Herz[3,4], Naoyuki Shono[2], Hiroshi Nakashima[2], Moritz Zaiss[3,5], E. Antonio Chiocca[2], Ouri Cohen[6], Matthew S. Rosen[1,7] and Christian T. Farrar[1]✉

Non-invasive imaging methods for detecting intratumoural viral spread and host responses to oncolytic virotherapy are either slow, lack specificity or require the use of radioactive or metal-based contrast agents. Here we show that in mice with glioblastoma multiforme, the early apoptotic responses to oncolytic virotherapy (characterized by decreased cytosolic pH and reduced protein synthesis) can be rapidly detected via chemical-exchange-saturation-transfer magnetic resonance fingerprinting (CEST-MRF) aided by deep learning. By leveraging a deep neural network trained with simulated magnetic resonance fingerprints, CEST-MRF can generate quantitative maps of intratumoural pH and of protein and lipid concentrations by selectively labelling the exchangeable amide protons of endogenous proteins and the exchangeable macromolecule protons of lipids, without requiring exogenous contrast agents. We also show that in a healthy volunteer, CEST-MRF yielded molecular parameters that are in good agreement with values from the literature. Deep-learning-aided CEST-MRF may also be amenable to the characterization of host responses to other cancer therapies and to the detection of cardiac and neurological pathologies.

The highly invasive nature of many cancer types and the toxicity of most systemic chemotherapies are great challenges that limit the effectiveness of cancer therapies. An especially promising therapeutic approach for overcoming these challenges is the use of oncolytic viruses, which selectively kill cancer cells[1]. Oncolytic viruses can generate progeny 'on site', which then spread throughout the tumour, reaching distal malignant cells. Hence, this represents a rather ideal strategy for treating invasive cancers such as glioblastoma[2]. Oncolytic viruses can also be 'armed' to express anticancer genes, and be employed for the targeted delivery of therapeutics[3,4]. In addition, oncolytic viruses can elicit a strong immune response against virally infected tumour cells, and were recently approved by the US Food and Drug Administration for the treatment of melanoma[5]. Non-invasive methods to image oncolytic viruses are essential for quantifying virus titres[6]. Moreover, molecular information provided during the course of therapy could provide detailed insights into both the tumour and the host responses, and help optimize virotherapy.

Chemical exchange saturation transfer (CEST) magnetic resonance imaging (MRI) has been shown to be sensitive to changes in tumour pathology[7]. CEST is a molecular imaging technique that uses radiofrequency (RF) pulses to saturate the magnetization of exchangeable protons on a variety of molecules, including proteins and metabolites[8]. During saturation of the solute exchangeable proton pool, chemical exchange with the bulk water protons acts as a saturation amplifier of the MRI water-signal change so that low concentrations of solute can be detected. The CEST contrast depends on the chemical exchange rate, which is pH sensitive, and on the volume fraction of the exchangeable proton pool, which is sensitive to protein and metabolite concentrations. The sensitivity of CEST MRI to pH and to protein and metabolite concentrations has been shown to be a potent tool for imaging a wide range of pathologies[9]. However, the clinical translation of CEST-MRI methods has been hindered by the semi-quantitative nature of the image contrast and the typically long image-acquisition times required.

Here we report the design of a deep-learning-based CEST-fingerprinting method for the quantitative and rapid molecular imaging of treatment responses to oncolytic virotherapy (OV) without the need for exogenous contrast agents. The technique is based on the selective magnetic labelling of exchangeable amide protons of endogenous proteins as well as of exchangeable protons of lipids and macromolecules (Fig. 1a), by using a pseudorandom and fast (3.5 min) RF-saturation pulse scheme (Fig. 1b) encoding the molecular properties into unique MR fingerprints[10]. Next, the acquired signals are rapidly decoded (94 ms) into four fully quantitative chemical-exchange and proton-concentration molecular maps, using a series of deep neural networks (Fig. 1c) trained with a dictionary of simulated MR fingerprints. The dictionaries are simulated for a range of semi-solid and amide chemical-exchange parameter values as well as water T_1 and T_2 relaxation times and B_0 magnetic-field-inhomogeneity values. The incorporation of the deep-learning-based reconstruction within the system architecture overcomes the highly multidimensional nature of this fingerprint-matching problem, and decouples and quantifies the different molecular properties. Moreover, we show that the

[1]Athinoula A. Martinos Center for Biomedical Imaging, Department of Radiology, Massachusetts General Hospital and Harvard Medical School, Charlestown, MA, USA. [2]Department of Neurosurgery, Brigham and Women's Hospital and Harvard Medical School, Boston, MA, USA. [3]Magnetic Resonance Center, Max Planck Institute for Biological Cybernetics, Tübingen, Germany. [4]Department of Biomedical Magnetic Resonance, University of Tübingen, Tübingen, Germany. [5]Department of Neuroradiology, Friedrich-Alexander Universität Erlangen-Nürnberg (FAU), University Hospital Erlangen, Erlangen, Germany. [6]Memorial Sloan Kettering Cancer Center, New York, NY, USA. [7]Department of Physics, Harvard University, Cambridge, MA, USA. ✉e-mail: operlman@mgh.harvard.edu; cfarrar@mgh.harvard.edu

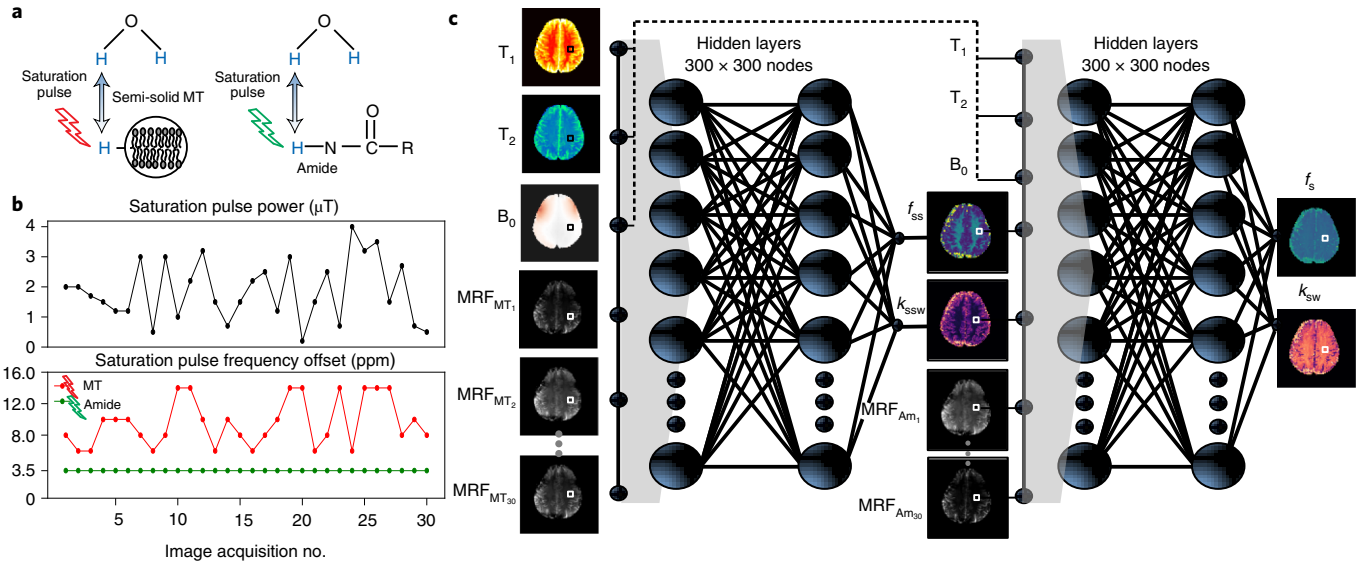

Fig. 1 | Schematic representation of deep-learning-boosted molecular MRI pipeline. a,**b**, The molecular information of the compounds of interest (semi-solid MT and amide) (**a**) is encoded into unique MR fingerprints using a series of saturation pulses described in **b**. This results in two sets of raw molecular-feature-embedded images (MRF_{MT} and MRF_{Am}). **c**, Quantitative image decoding. The encoded image sets as well as quantitative water-pool and field homogeneity maps (T_1, T_2, B_0) are input sequentially into two reconstruction deep neural networks, ultimately yielding quantitative molecular maps depicting the proton exchange rate (k_{ssw}, k_{sw}) and the volume fraction (f_{ss}, f_s) for the semi-solid and amide pools, respectively.

reconstruction time is five orders of magnitude faster than traditional MR-fingerprinting reconstruction.

We evaluated the approach in mice undergoing OV treatment. The resulting quantitative maps allowed for the early detection of apoptosis induced by OV. The method was translated to a clinical MRI scanner and used to image a healthy human subject. The quantitative molecular maps obtained are in good agreement with the relevant literature.

Results

We evaluated the suitability of the deep-learning-boosted molecular MRI method for monitoring OV treatment responses in a longitudinal animal study. We used an orthotopic mouse model of a U87ΔEGFR human glioblastoma ($n=16$, 25% served as control). Imaging was performed at baseline (8–11 d post tumour implantation) as well as at 48 and 72 h post OV treatment.

The quantitative exchange parameter maps obtained for a representative OV-treated mouse can be seen in Fig. 2a–c, and the quantitative analysis for all OV-treated mice is presented in Fig. 2d. For all examined molecular parameters, the null hypothesis, claiming that the tumour, contralateral and apoptotic region at all time points are from the same distribution and have equal means was rejected by one-way analysis of variance (ANOVA) ($F_{(7,64)}=45.87$, 18.24, 95.09 and 13.14 for the amide proton volume fraction and exchange rate (f_s, k_{sw}) and the semi-solid proton volume fraction and exchange rate (f_{ss}, k_{ssw}), respectively; $P<0.0001$ in all cases). All group comparison analyses were performed using a two-sided Tukey's multiple comparisons test (see Methods).

Before OV inoculation, the semi-solid volume fraction (f_{ss}) was found to be significantly decreased in the tumour compared with the contralateral tissue ($P<0.0001$, $n=11$), in agreement with reports of similar decreases in the tumour f_{ss}[11–13]. The amide proton volume fraction (f_s) was significantly decreased in the tumour compared with the contralateral tissue ($P<0.0001$, $n=11$). Notably, a previous study reported that malignant gliomas are highly cellular[14], whereas more recent studies reported a similar total protein concentration in the tumour and normal brain tissue[11,15]. The f_s decrease shown here can be explained by the high tumour oedema (as indicated by the highly elevated T_2 values, Fig. 2a and Supplementary Fig. 1), diluting the protein concentrations. In contrast, the tumour amide proton exchange rate (k_{sw}) was significantly increased ($P<0.01$, $n=11$), indicative of increased intratumoural pH in agreement with literature reports[16]. Forty-eight hours following OV (Fig. 2b), the centre of the tumour presented significantly lower amide proton concentration compared with the contralateral ($P<0.0001$, $n=10$ contralateral, $n=9$ tumour centre) and tumour rim regions ($P<0.0001$, $n=10$ tumour rim, $n=9$ tumour centre). The same trend was observed at 72 h post inoculation ($P<0.0001$, $n=7$). The amide proton exchange rate at 48 h following OV was significantly lower in the tumour centre compared with the contralateral ($P=0.0197$, $n=10$ contralateral, $n=9$ tumour centre) and tumour rim regions ($P<0.0001$, $n=10$ tumour rim, $n=9$ tumour centre). A similar trend was observed at 72 h post inoculation ($P<0.0001$, $n=7$). The decrease in both amide proton exchange rate (which is sensitive to pH) and volume fraction (which is sensitive to protein concentration) suggests an apoptotic event in these areas as it is known to inhibit protein synthesis[17] and decrease cytosolic pH[18]. Interestingly, the semi-solid exchange rate was significantly decreased in the tumour compared with the contralateral region at all time points ($P<0.001$, $P<0.0001$ and $P<0.01$ for baseline ($n=11$), 48 h ($n=10$ contralateral and tumour, $n=9$ apoptotic) and 72 h ($n=7$) post inoculation, respectively). This is attributed to the change in lipid composition of the tumour cell membranes compared to healthy brain tissue[19], which alters the base-catalysed exchange rate constant of the semi-solid protons[20]. Thus, the semi-solid proton exchange rate depends not only on pH, but also on the lipid/macromolecule composition, leading to a decreased exchange rate at baseline despite the increased pH. In contrast, for amide exchangeable protons from small mobile proteins with simple aqueous chemical environments, the base-catalysed exchange rate constant remains constant, and the exchange rate is dependent only on the pH. The reproducibility of the proposed imaging method was confirmed by the lack of statistically significant differences in the parameter values of the contralateral region over-time (amide proton volume fraction: $P>0.78$ and

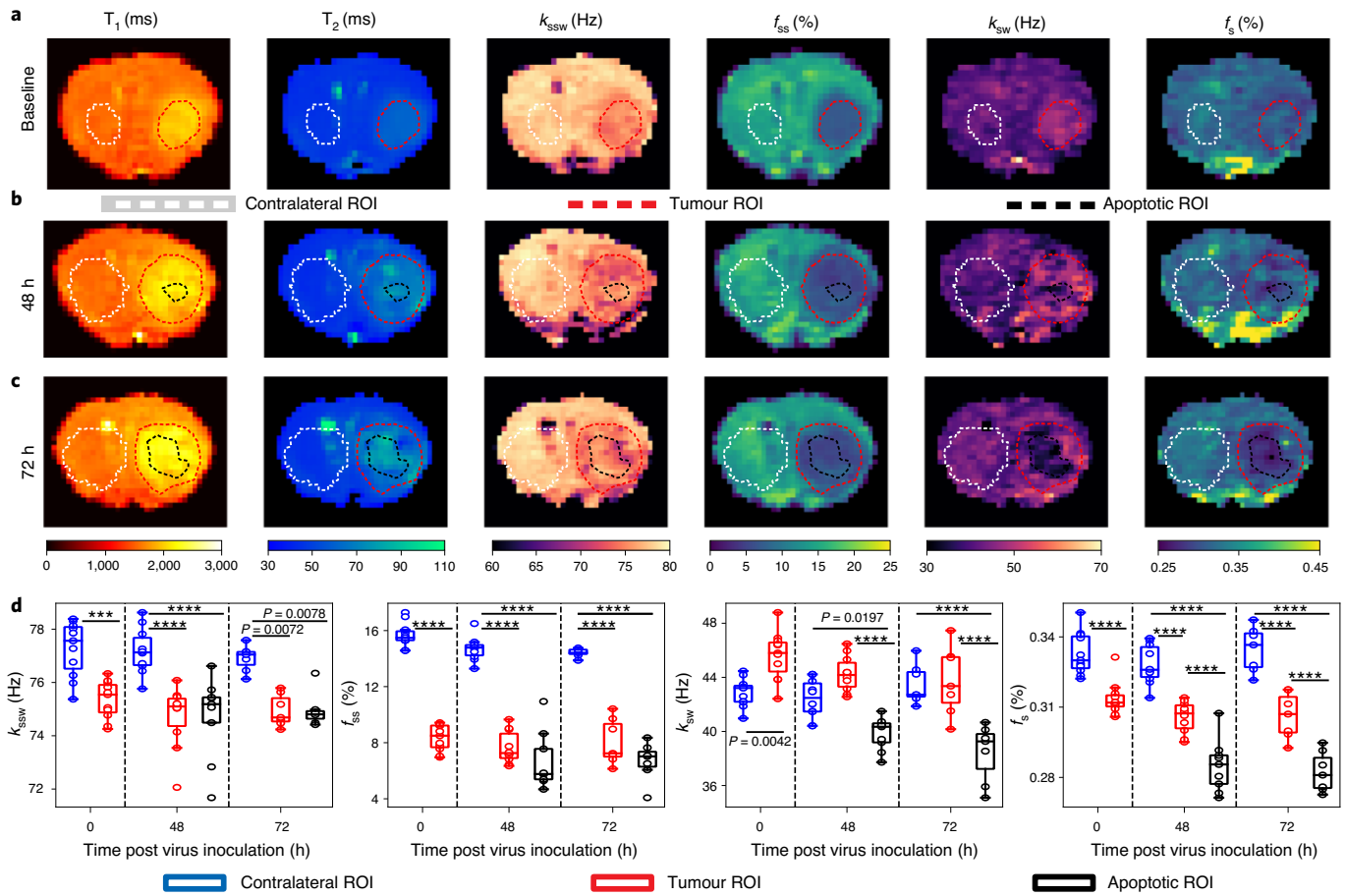

Fig. 2 | Quantitative molecular images of a representative OV-treated mouse. a–c, Before inoculation (**a**), the tumour semi-solid (f_{ss}) and amide (f_s) proton concentrations decreased, consistent with increased oedema. The tumour amide proton exchange rate (k_{sw}) increased, indicative of increased intratumoural pH. Forty-eight (**b**) and 72 (**c**) hours following OV, the tumour centre presented lower f_s and k_{sw} compared with the tumour rim and the contralateral region, indicative of apoptosis. **d**, Quantitative group comparison, demonstrating the statistical significance of the described phenomena using one-way analysis of variance (ANOVA) ($F_{(7,64)} = 45.87$, 18.24, 95.09 and 13.14 for f_s, k_{sw}, f_{ss} and k_{ssw}, respectively; $P < 0.0001$ in all cases). *P* values were determined by one-way ANOVA followed by correction for multiple comparisons using a two-sided Tukey's multiple comparisons test, and are indicated in **d** for baseline ($n = 11$ animals, all regions), 48 h ($n = 10$ animals, contralateral and tumour; $n = 9$ animals, apoptotic) and 72 h ($n = 7$ animals, all regions) post inoculation time points. ***$P < 0.001$; ****$P < 0.0001$. In all box plots: the central horizontal lines represent median values, box limits represent upper (third) and lower (first) quartiles, whiskers represent 1.5× the interquartile range above and below the upper and lower quartiles, respectively, and all data points are plotted. The quantitative molecular-imaging experiment was performed for all animals, yielding similar results (per control/treated group association); see additional examples in Supplementary Figs. 2, 5 and 11.

proton exchange rate: $P > 0.86$; semi-solid macromolecules volume fraction: $P > 0.41$ and proton exchange rate: $P > 0.49$; minimal *P* value is mentioned for baseline ($n = 11$ all regions), 48 h ($n = 10$ contralateral and tumour, $n = 9$ apoptotic) and 72 h ($n = 7$, all regions) post inoculation).

We next validated the MRI-based molecular findings using histology and immunohistochemistry (IHC). Formalin-fixed paraffin-embedded tissue sections were extracted from six randomly chosen mice. A representative histology/IHC image-set and its comparison to the corresponding MR image-set can be seen in Fig. 3, and all stained mice can be seen in Supplementary Figs. 2, 3 and 4. HSV-1 antigens (indicating the viral biodistribution) were detected by IHC (Fig. 3e) and were located within the tumour boundaries (Fig. 3f) marked by the hematoxylin and eosin (H&E) stained region. The H&E stained region was in good agreement with the region of decreased MR semi-solid proton volume fraction (Fig. 3b). A well-defined region of IHC-positive cleaved caspase-3 fragment indicative of cell apoptosis was observed (Fig. 3g), in good agreement with the region of reduced amide proton exchange rate (Fig. 3c). The Coomassie Blue stained image indicated that a reduction in protein concentration occurred at the tumour centre (Fig. 3h), in a region similar to the apoptotic one (Fig. 3g) and in agreement with the region of decreased amide proton volume fraction (Fig. 3d). Staining for cell proliferation using Ki-67 provided additional validation of these findings, where decreased cell proliferation was observed in OV-infected regions (Supplementary Fig. 4).

The quantitative maps obtained for a representative non-virally treated control mouse and the quantitative analysis of the entire control group can be seen in Supplementary Fig. 5. The trends in the molecular exchange parameters at baseline were similar to that occurring in the OV-treated group (Fig. 2a) as expected, namely an apparent decrease in the amide proton volume fraction, semi-solid proton volume fraction and semi-solid proton exchange rate at the tumour region, accompanied by a simultaneous increase in the tumour amide proton exchange rate. We note that although the effect was statistically significant for the semi-solid exchange rate and volume fraction (one-way ANOVA ($F_{(5,12)} = 9.598$, 100.8, $P = 0.0007$, $P < 0.0001$, respectively), with correction for multiple comparisons using a two-sided Tukey's multiple comparisons test $P < 0.05$, $P < 0.0001$, respectively; $n = 3$), it was not significant

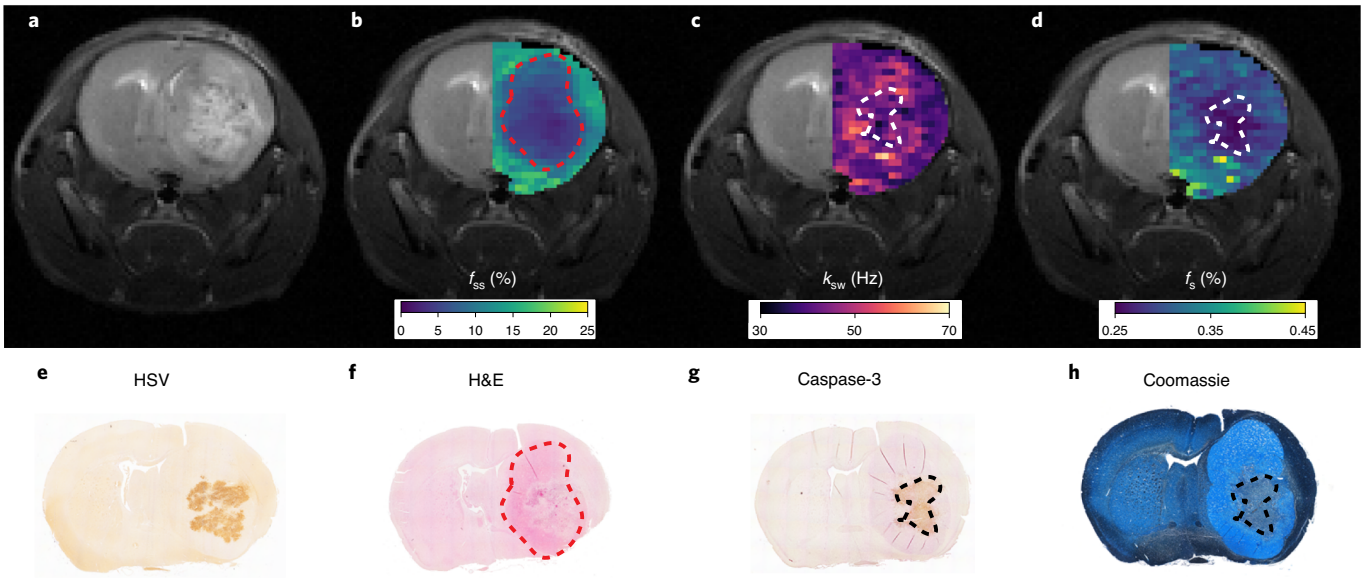

Fig. 3 | Histology validation. a, T_2-weighted image of an OV-treated mouse 72 h after virus inoculation. **b**, Semi-solid macromolecules proton volume fraction (f_{ss}) map overlaid atop the T_2-weighted image at the ipsilateral side. **c**,**d**, Similarly overlaid amide proton exchange rate (k_{sw}) and amide proton volume fraction (f_s) maps, respectively. **e**, Immunohistochemistry image stained for the presence of Herpes simplex virus (HSV) (brown). **f**, H&E-stained image showing the tumour location (pink). **g**, Caspase-3 immunohistochemistry image showing the apoptotic tumour region (brown). **h**, Coomassie Blue-stained image showing reduced protein concentration in the apoptotic tumour centre. The dashed lines in **b**–**d** and **f**–**h** generally depict the tumour (**b**,**f**) and the borders of the apoptotic (**c**,**d**,**g**,**h**) regions, respectively. A total of 6 random mice (3 OV-treated and 3 control) underwent the histology procedure, yielding similar results (per control/treated group association); also see Supplementary Fig. 2.

for the amide proton volume fraction and exchange rate (one-way ANOVA ($F_{(5,12)}=3.804$, 0.8968, $P=0.0269$, $P=0.5136$, respectively), and with correction for multiple comparisons using a two-sided Tukey's multiple comparisons test $P>0.05$; $n=3$). As expected, no apoptotic region, manifested as a region of decreased amide exchange rate, was detected at the later time points (Supplementary Fig. 5b,c). This molecular MR-based finding was in agreement with the histology/IHC images of the control mice group (Supplementary Fig. 2), where no HSV-1 antigens were detected, no IHC-positive cleaved caspase-3 fragments were observed (but only haematoxylin counterstaining) and no reduction in protein concentration at the tumour centre (Coomassie Blue) was visible.

A combined display and statistical comparison between the OV-treated and control mice groups for each of the therapeutic time points is available in Supplementary Fig. 6. As expected, no statistically significant differences were observed for the tumour regions of interest (ROI) (without apoptosis) between the virotherapy and control groups (corrected for multiple comparisons using a two sided Tukey's multiple comparison test, k_{ssw}: $P=0.5759$, 0.9481, 0.1995; f_{ss}: $P=0.9862$, 0.4053, 0.9999; k_{sw}: $P=0.1665$, 0.9355, 0.3188; f_s: $P=0.7094$, 0.1524, 0.8259 for the baseline ($n=3$ control, $n=11$ virotherapy group), 48 h ($n=3$ control, $n=10$ virotherapy group) and 72 h ($n=3$ control, $n=7$ virotherapy group) post inoculation times, respectively). Similarly, no statistically significant differences were observed for the contralateral ROI between virotherapy and control groups for all cases, except for the k_{ssw} at 72 h post inoculation (corrected for multiple comparisons using a two-sided Tukey's multiple comparison test, k_{ssw}: $P=0.2104$, 0.9953, 0.0129; f_{ss}: $P=0.998$, 0.8847, 0.2933; k_{sw}: $P=0.9989$, 0.2905, 0.9999; f_s: $P=0.992$, 0.4898, 0.9999 for the baseline ($n=3$ control, $n=11$ virotherapy group), 48 h ($n=3$ control, $n=10$ virotherapy group) and 72 h ($n=3$ control, $n=7$ virotherapy group) post inoculation time points, respectively). Finally, a statistically significant difference in the exchange parameter values was observed between both the apoptotic ROI (48 h, $n=9$; 72 h, $n=7$) and the contralateral/tumour ROIs for the virotherapy mice group, as well as between the virotherapy group apoptotic ROI and the contralateral/tumour ROIs for the control mice group (see Supplementary Fig. 6 for additional information).

The same deep-learning-boosted molecular MRI method was then adapted to a clinical human MRI scanner using the same encoding–decoding procedure (Fig. 1) and only minimal modifications to the pulse sequence to minimize tissue RF-power deposition (see Methods and Supplementary Table 1 for additional details). A healthy volunteer was recruited and imaged at 3 T, following Institutional Review Board (IRB) approval and informed consent. The resulting molecular maps (Fig. 4) yielded semi-solid proton volume fractions of $9.4\pm3.0\%$ and $4.2\pm4.4\%$ for white matter (WM) and grey matter (GM) regions, respectively. The elevated semi-solid proton volume fraction observed in WM compared with GM is consistent with the higher lipid/myelin content of WM. The resulting semi-solid exchange rates were: WM, 14.0 ± 6.9 Hz; GM, 35.1 ± 15.4 Hz. Since no difference in pH is expected between WM and GM, the difference in semi-solid exchange rates observed for WM and GM again indicates the sensitivity of the semi-solid base-catalysed exchange rate constant to the lipid composition, as also observed in the mouse tumour model (Fig. 2d). Both semi-solid exchange parameter values were in good agreement with previous studies (volume fractions: $13.9\pm2.8\%$ and $5.0\pm0.5\%$, exchange rates: 23 ± 4 and 40 ± 1 Hz for the WM and GM, respectively)[21] despite the substantial variance existing in the literature (Supplementary Table 2). The measured amide proton WM/GM exchange rates (42.3 ± 2.9 Hz/34.6 ± 9.5 Hz) were in good agreement with previous water-exchange spectroscopy measurements in rat models (28.6 ± 7.4 Hz)[22]. All data are presented as mean ± standard deviation.

Discussion

Apoptosis is considered an early predictor of cancer therapy outcome, as it manifests before any visible reduction in tumour volume[23,24]. This has motivated the pursuit of imaging methods capable of apoptosis detection[25]. Previous methods developed for the detection of apoptosis relied on pH-sensitive dual-emission fluorescent

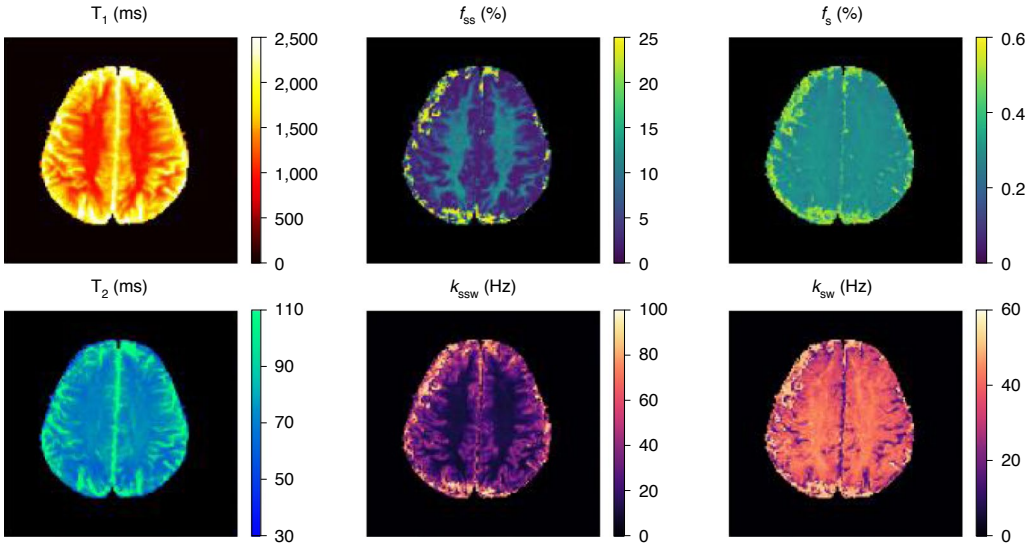

Fig. 4 | Assessment of deep-learning-boosted molecular MRI in a healthy volunteer at 3 T. The resulting white/grey matter semi-solid volume fractions (9.4 ± 3.0%/4.2 ± 4.4%) and exchange rates (14.0 ± 6.9 Hz/35.1 ± 15.4 Hz) were in good agreement with the literature (see Supplementary Table 2). The white/grey matter amide proton exchange rates (42.3 ± 2.9 Hz/34.6 ± 9.5 Hz) were in good agreement with previous water-exchange spectroscopy measurements in rat models[22].

probes[18], caspase-3-targeted optical-imaging probes[26,27], as well as radiolabelled Annexin V (ref. [28]) and duramycin[29] positron emission tomography (PET) and single-photon emission computed tomography (SPECT) imaging probes that respectively target phosphatidylserine or phosphatidylethanolamine expressed on the surface of apoptotic cells. Additional methods relied on changes in the endogenous lipid proton MR spectroscopy[23] or high-frequency ultrasound signals[30]. However, PET and SPECT require the use of ionizing radiation and exogenous probes, whereas optical and ultrasound-based methods suffer from limited tissue penetration (and hence are unsuitable for clinical neurological applications). In contrast, MRI provides a safe and clinically relevant alternative. Although water T_1/T_2 mapping provides a useful means for detecting oedema and tumour formation (in some cases visually indicating a therapeutic effect), it is insufficient for the accurate and specific detection of apoptotic responses (Supplementary Fig. 1). The intuitive method of choice for MR-based molecular imaging of apoptosis is MR spectroscopy[23]. However, MR spectroscopy is limited by poor spatial resolution and exceedingly long scan times owing to its low sensitivity[31]. Diffusion-weighted MR imaging was shown to be correlated with apoptosis processes[24]. However, it has low sensitivity and may result in false-positive apoptosis indications because numerous other biological and pathological processes induce diffusion changes[32]. Exogenous contrast agents, such as gadolinium or superparamagnetic iron oxides, can be administered for MR T_1/T_2-based apoptosis detection after labelling the contrast agent with an appropriate targeting probe[33]. However, owing to difficulties in the delivery of large, targeted contrast agents across the blood–brain barrier and recent concerns about the risk of adverse events when using metal-based probes for contrast enhancement, an endogenous contrast-based method would constitute a favourable alternative.

CEST-MRI of endogenous amide protons has been extensively explored for pH-weighted imaging; hence, it constitutes a potential tool for apoptosis detection. The CEST pH-imaging ability was initially demonstrated in acute stroke rodent models[34] and later translated into clinical scanners for human subjects[35]. However, such studies typically use the magnetization transfer ratio asymmetry (MTR_{asym}) as an analysis metric, which is affected by the proton exchange rate and volume fraction, the aliphatic proton pools (rNOE), the water T_1 and T_2 relaxation times and the saturation pulse properties[36,37]. As a result, pathology-related changes in the water-pool T_1 and T_2 and semi-solid and aliphatic proton-pool properties may challenge the correct interpretation of a qualitative CEST-weighted image[38–40] (Supplementary Fig. 7a). Thus, this metric does not provide direct and quantitative information regarding the contribution of each of these components to the detected CEST signal change. In particular, in OV-treated mice, the MTR_{asym} values were significantly higher at the tumour rim and at the apoptotic centre ROIs than at the contralateral ROIs (Supplementary Fig. 8d). However, no statistically significant differences were calculated between the apoptotic and tumour ROIs at 48 h and 72 h post inoculation ($P = 0.8354$, $n = 10$ tumour, $n = 9$ apoptotic, and $P = 0.8572$, $n = 7$, respectively; one-way ANOVA with correction for multiple comparisons using two-sided Tukey's test). Although the MTR_{asym} seeks to obtain information on the amide proton pool, it might have been contaminated, in the virotherapy case, by the increase in the water T_1/T_2 relaxation times (Supplementary Fig. 1) and the decrease in the rNOE signal in the tumour (Supplementary Fig. 9d).

Although previous studies[41] have reported a decrease in the tumour amide proton transfer (APT)-weighted CEST signal in response to chemotherapy, they could not determine whether the signal change was the result of a decrease in intratumoural pH or only a reduction in protein concentration. Recently, the relative contributions of intratumoural pH and protein concentration changes in generating the tumour APT-weighted CEST contrast were reported[42]. However, to obtain this estimation, additional information from ex vivo histology measurements (Coomassie staining) was required. In contrast, the method that we report here is fully quantitative and suitable in vivo, and it generates separate maps for each biophysical property. It can thus confirm (or shed new light on) previously hypothesized mechanisms underlying treatment responses. Moreover, as the deep-learning-boosted molecular MRI method does not require any additional information from invasive histology, and its acquisition and reconstruction times are short, it is clinically relevant, potentially providing the physician with a means for the longitudinal assessment of the biophysical and molecular characteristics of treated tumours.

Although the various contributions of different proton pools to the CEST contrast can be separated out by using the previously suggested Lorentzian fitting approach[43], the output in this case is still a single pool-weighted image for each molecular compound, which cannot fully distinguish between pH changes and protein concentration or magnetic relaxation effects (Supplementary Fig. 7b–f). Therefore, in the presence of competing molecular mechanisms, the resulting 'CEST-weighted' images will not necessarily be correlated with changes in either pH or protein content. This is demonstrated in the conventional Lorentzian-fitted parameters obtained for the OV-treated mice shown in Supplementary Fig. 9d. For example, despite the significant increase in exchange rate and the decrease in proton volume fraction observed in the tumour for the quantitative CEST fingerprinting maps at baseline (Fig. 2a,d), no significant difference was observed between contralateral and tumour tissues for the conventional Lorentzian-fitted amide amplitude (Supplementary Fig. 9d). This is attributed to the fact that the CEST contrast (even if separated out from other pools, such as MT and rNOE) is proportional to the product of the proton exchange rate and concentration. In these challenging cases, a quantitative approach such as MR fingerprinting[10] is attractive.

MR fingerprinting provides good accuracy, and correlates well with ground truth for two-solute-pool imaging scenarios (Supplementary Fig. 10 and Table 3). Nevertheless, a straightforward implementation of a single CEST MR fingerprinting encoding scheme[44] and the traditional correlation-based reconstruction provide a poor estimation of the molecular properties in in vivo diseases such as cancer (Supplementary Figs. 7g–l and 11). This stems from the highly multidimensional parameter space involved and the simultaneous parameter variations in multiple molecular pools. The sequential architecture of the deep-learning-boosted CEST MR fingerprinting approach overcomes all of the above challenges. Specifically, our approach first uses a semi-solid macromolecule-selective encoding to properly isolate and quantify the properties of this pool (Fig. 1b). Only then, using a much smaller parameter space, are the amide proton properties mapped with the use of an amide-oriented encoding schedule (Fig. 1b). The ability of the sequential deep networks to computationally manage large numbers of parameters allows us to properly include the effects of the water-pool relaxation properties and of magnetic field inhomogeneities as inputs to both neural networks. Supplementary Figs. 7m–r and 11 further show that sequentially 'nailing down' each pool parameter before classifying the next pool is indeed an essential strategy for overcoming this highly multidimensional challenge. Moreover, the use of neural networks for image reconstruction allows for continuous parameter classification, instead of the discrete set of values obtained when performing traditional correlation-based matching, where the matching dictionary contains only certain discrete parameter values. Finally, the image reconstruction time is 88,085 times shorter for the proposed method compared with standard MR fingerprinting (94 ms instead of 2.3 h for a 128 × 128 pixel image). Our use of neural networks in this fingerprinting approach differs from the use of neural-network-based nonlinear-regression methods, which were recently used for the extraction of proton-pool Lorentzian parameters[45] and for the quantification of phosphocreatine in leg muscle[46] from conventional CEST *Z*-spectra. In particular, the fingerprinting method has previously been shown to have substantially improved parameter discrimination compared with CEST *Z*-spectra[44]. The combination of the fingerprinting method with the sequential deep networks is critical for characterizing the much more complicated tumour tissue pathology, where a large number of different molecular parameters are all changing and must be accounted for.

In terms of image acquisition time, we note that the requirement of static magnetic field (B_0) and water-pool relaxation parameter maps (Fig. 1c) as network inputs prolongs the total scan time. However, all three maps can be obtained in approximately 30 s by using the previously established water-pool T_1 and T_2 MR fingerprinting method[10]. Thus, with a 3.5 min acquisition time for the amide and semi-solid proton pools, the total acquisition time is less than 5 min. Notably, it is highly desirable to convert the single-slice method implemented here into a 3D protocol, providing whole brain coverage. This could be pursued by combining the CEST MR fingerprinting approach with fast volumetric-acquisition protocols, such as 3D-snapshot CEST[47], multiband simultaneous multi-slice echo-planar imaging (EPI)[48] or multi-inversion 3D EPI[49].

In future, ^{31}P imaging should be included for the determination of intracellular pH to further validate the CEST-MRF pH-biomarker capabilities. In addition, to improve the biophysical parameter discrimination ability and reduce quantification variabilities, the CEST-MRF acquisition schedules should be further optimized by implementing either an exhaustive search, numerical optimization techniques or machine-learning-based optimization algortihms[50–52].

Outlook

Non-invasive apoptosis monitoring could become beneficial for a variety of clinically relevant scenarios characterized by irregular apoptosis levels. This includes liver disease[53], transplant rejection imaging[54], and Alzheimer's, Parkinson's and Huntington's diseases[55]. More generally, deep-learning-boosted molecular MRI is directly applicable to any semi-solid macromolecule and amide proton CEST imaging application. This includes pH imaging for stroke detection and ischaemic penumbra characterization[34], differentiation of ischaemia from hemorrhage[56], cancer grading[57], detection of biological therapeutics engineered with CEST reporter genes[58–60], differentiation of radiation necrosis and tumour progression[61], detection and evaluation of lesions in multiple sclerosis[62] and characterization of neurodegenerative diseases[63]. Furthermore, future work could optimize and modify the encoding scheme (Fig. 1b) so that additional metabolites (such as creatine, glutamate and glucose) and molecular information could be quantitated.

Methods

In vivo preclinical MRI acquisition. The mouse imaging study was conducted using a 7 T preclinical MRI scanner (Bruker Biospin). The mice were anaesthetized using 0.5–2% inhaled Isoflurane (Harvard Apparatus) during the imaging, and the respiration rate was continuously monitored using a respiratory pillow (SA Instruments). Two chemical exchange saturation transfer (CEST) MR fingerprinting acquisition protocols were employed sequentially (105 s each, Fig. 1a,b), designed for encoding the semi-solid macromolecule (denoted as MT, magnetization transfer) and amide information into unique trajectories. The exchangeable amide proton signals of endogenous mobile proteins have a chemical shift of 3.5 ppm with respect to water and a relatively narrow resonance linewidth due to the rapid molecular motion. In contrast, the exchangeable protons on lipids and large macromolecules have a chemical shift of approximately −2.5 ppm from water and a broad resonance linewidth due to the slow molecular motion. The first protocol was aimed at magnetic labelling of the MT pool, varying the saturation pulse frequency offset between 6 and 14 ppm (to avoid amide/amine/aliphatic nuclear Overhauser effect (NOE) contributions) and the saturation pulse power between 0 and 4 μT. The second protocol was aimed at magnetic labelling of the amide pool (in the presence of MT), using the same saturation pulse power schedule but with a fixed saturation pulse frequency offset at 3.5 ppm. Both protocols had repetition time/echo time (TR/TE) = 3,500/20 ms, a flip angle of 90°, a continuous saturation pulse of 2,500 ms and a spin-echo echo-planar-imaging (SE-EPI) readout. T_1 maps were acquired using the variable repetition-time rapid acquisition with relaxation enhancement (RARE) protocol, with TR = 200, 400, 800, 1,500, 3,000 and 5,500 ms, TE = 7 ms, RARE factor = 2, acquisition time = 364.8 s. T_2 maps were acquired using the multi-echo spin-echo protocol, TR = 2,000 ms, 25 TE values between 8 and 200 ms and acquisition time = 128 s. Static magnetic field (B_0) maps were acquired using the water saturation shift referencing (WASSR) protocol[64], employing a saturation pulse power of 0.3 μT, TR/TE = 8,000/20 ms, flip angle = 90°, saturation duration = 3,000 ms and a saturation pulse frequency offset varying between −1 and 1 ppm in 0.1 ppm increments, acquisition time = 176 s. A traditional full *Z*-spectrum CEST scan was performed for comparison, using an SE-EPI sequence with TR/TE = 8,000/20 ms, flip-angle = 90° and pre-saturation pulses of 0.7 μT and 3,000 ms at −7 to 7 ppm frequency offsets with 0.25 ppm increments and a no-saturation reference image, acquisition time = 464 s. The field of view (19 mm × 19 mm × 1 mm) and

image resolution (297×297×1000 μm³) were identical for all scans besides a high-resolution (148×148×1,000 μm³) T_2-weighted scan (TR/TE = 2,000/60 ms), taken as reference. The total acquisition time per mouse, including comparison scans, was 22 min and 22.8 s.

CEST MR fingerprinting dictionary generation. Dictionaries of CEST signals were generated, simulating the expected trajectories for more than 70 million tissue parameter combinations, as a response to the two molecular-information-encoding acquisition protocols (Fig. 1a,b). The simulations were carried out using a numerical solution of the Bloch-McConnell equations, implemented in MATLAB R2018a (MathWorks) and C++ (ref. [44,65]). Generating all dictionaries used in this work took a total of 62.5 h, using a computer cluster employing 56 CPUs. Detailed dictionary properties can be found in Supplementary Table 1.

Quantitative image decoding using deep reconstruction networks. To avoid the exceedingly long dictionary matching time required for conventional correlation-based MR fingerprinting (for example, 2.31 h for reconstructing a single 128×128 pixels image set out of >70 M dictionary entries, using a 12 GiB Intel Xeon E5607 CPU-equipped Linux desktop computer) and to improve the multiparameter reconstruction ability (Supplementary Fig. 7g–r), image decoding was performed using a series of two deep reconstruction networks (DRONEs)[66]. Each neural network was composed of four layers, including 300×300 neurons in the two hidden layers (Fig. 1c). A rectified linear unit and a sigmoid were used as the hidden and output activation functions, respectively. Network training was performed using the synthesized dictionary data, with the trajectories normalized to zero mean and unit standard deviation along the temporal axis[67]. The adaptive moment estimation (ADAM) optimizer[68] was used, with a learning rate = 0.0001, minibatch size = 256 and the mean squared error defined as the loss function. To avoid over-fitting, 10% of each dictionary (Supplementary Table 1) was excluded from training and was used to assess when to stop the training ('early stopping'). To promote robust learning, white Gaussian noise was injected into the dictionaries[69]. At the reconstruction step, the pixelwise signal trajectories from the 30 images acquired using the MT-specific MR fingerprinting schedule were normalized along the temporal axis[67] and input to the first DRONE, together with the pixelwise water T_1, T_2 and B_0 values (normalized by subtracting the mean and dividing by the standard deviation of the training dictionary parameters). The two MT exchange parameter output maps, together with the water pool T_1 and T_2 relaxation and B_0 parameter maps, were then input into the second DRONE, together with the pixelwise signal trajectories from the 30 images acquired using the amide-pool MR fingerprinting schedule (normalized similarly as the MT schedule images). The neural networks were implemented in Python 3.6 using TensorFlow 1.4.1 on a desktop computer equipped with an Intel Xeon E5607 CPU and an NVIDIA TITAN Xp GPU.

Animal model. All experimental protocols were approved by the Institutional Animal Care and Use Committees (IACUC) of the Brigham and Women's Hospital (BWH). All animal experiments were carried out in accordance with approved IACUC ethical guidelines and regulations. Sixteen female athymic mice (BALB/c, nu/nu; 6–8 weeks old) were purchased from Envigo. U87ΔEGFR (100,000 cells) were implanted stereotactically with a Kopf stereotactic frame (David Kopf Instruments) in the right frontal lobe of the mice (ventral 3.0 mm, rostral 0.5 mm and right lateral 2.0 mm from bregma). Tumour burden was not measurable for the intracranial tumour models used; instead, two criteria were approved by the the institutional (BWH) IACUC, which were followed and not exceeded in the study: (1) Permanent postural deficits, abnormal grooming behaviour or sustained neurological symptoms (seizures, tremors, circling), (2) Deficiencies in eating, drinking or moving in the cage; loss of weight (>10% pre-surgical weight) that does not correct within 5 d after providing Hi-Cal boost diet; extensive loss of weight (20%) since last monitoring event; BCS index <2; comatose or moribund state compared to prior daily examination. Imaging was performed at 8–11 d post implantation (the mice weighed 19–23 g) using a 7 T preclinical MRI (Bruker Biospin). Next, a Herpes simplex virus type I-derived oncolytic virus, NG34 (ref. [70]), was inoculated intratumourally to 12 of the mice (the others served as control), and the imaging was repeated 48 and 72 h later. The mice were anaesthetized using 0.5–2% inhaled Isoflurane (Harvard Apparatus) during the imaging, and the respiration rate was continuously monitored using a mechanical sensor (SA Instruments). Following the last imaging time point, the mice were euthanized using CO_2 inhalation and the brain tissue was extracted, formalin-fixed and paraffin-embedded for histology and immunohistochemistry. An additional female C57/BL6 tumour-bearing mouse (6–8 weeks old, without treatment) weighing 19–23 g was used for demonstrating the differences between the proposed and previously suggested molecular CEST MRI methods (Supplementary Fig. 7). Four mice died before the planned termination point (two between the baseline and 48 h scan and two between the 48 h and 72 h scan).

L-arginine phantom study. To further evaluate the accuracy of the method, we have implemented the core neural-network reconstruction element on the same phantom data used for validating and establishing previous correlation-based CEST MRF reports[44,65]. The same original dictionary depicted in ref. [44] was used for the network training, while 10% of the simulated signals was excluded and used to prevent over-fitting. The experimental CEST MRF signal trajectories used for testing the accuracy of the method were obtained by scanning four L-arginine phantoms (at 4.7 T, Bruker) containing 12 combinations of different proton exchange rates and concentrations. The resulting accuracy of the deep-learning-based parameter maps was evaluated based on the known L-arginine concentrations and the steady-state quantification of exchange using saturation power (QUESP) method[71]. The results were compared to the accuracy and values obtained using the standard dictionary matching based on conventional correlation of signal trajectory. Additional details are available in Supplementary Table 3 and Fig. 10.

Iohexol phantom study. An additional phantom imaging study was performed using Iohexol[72–75], which contains two exchangeable amide protons at a chemical shift similar to the in vivo one (4.3 ppm). Two amide-based phantoms were created at Iohexol concentrations of 20–80 mM, titrated to pH levels of 6.72–7.21. The phantoms were imaged using a 4.7 T scanner (Bruker Biospin) at room temperature. The resulting accuracy of the deep-learning-based parameter maps was evaluated based on the known Iohexol concentrations and measurement of the exchange rates using the steady-state quantification of exchange using saturation power (QUESP) method[71]. Additional details are available in Supplementary Table 4 and Fig. 13.

Statistical analysis. Group comparative analyses were carried out using one-way ANOVA, followed by correction for multiple comparisons using a two-sided Tukey's multiple comparisons test in Prism 6 (GraphPad). Two-tailed *t*-test and Pearson correlation coefficients were calculated using the open source SciPy scientific computing library for Python[76]. Absolute percentage error was defined as |true value − estimated value|/(true value) × 100 (Supplementary Table 3 and Fig. 10). Differences were considered significant at $P < 0.05$. In all box plots, the central horizontal lines represent median values, box limits represent upper (third) and lower (first) quartiles, whiskers represent 1.5× the interquartile range above and below the upper and lower quartiles, respectively, and all data points are plotted. Column scatter plots (Supplementary Figs. 5 and 6) include horizontal and vertical lines representing the group mean and standard deviation, respectively. The following two exclusion criteria were imposed: unsuccessful tumour implantation (occurred in 1 mouse out of 16); corrupted image data (occurred in 2 image sets out of 39, potentially due to RF coil/transmitter error).

Immunohistochemistry. Mouse brain tissues were fixed with 10% neutralization buffer and embedded in paraffin by Servicebio. The embedded samples were sectioned and processed sequentially with xylene, ethanol and distilled water to attain deparaffinization and rehydration. The following procedures were performed separately for each staining.

Immunohistochemistry. Histology slides were kept in citrate buffer (pH 6) heated to sub-boiling temperature for 20 min and cooled at room temperature for 30 min. After treating the slides with 3% hydrogen peroxide in distilled water to lower intrinsic peroxidase activity, the slides were incubated with 2% normal goat serum/20 mM Tris-buffered saline, 0.05% Tween-20 (TBST) to block unspecific antibody binding. Slides were incubated with primary antibodies against HSV 1 (B0114, Dako; 1:100 dilution), cleaved caspase-3 (9579, Cell Signaling Technology; 1:150) or Ki-67[77] (MA5-14520, Invitrogen; 1:200 dilution) diluted with TBST as recommended by the manufacturer. The MACH4 Universal HRP-Polymer (M4U534, Biocare Medical) and Metal Enhanced DAB Substrate Kit (34065, Thermo Fisher Scientific) were used to induce chromogenic reaction for detection. Additionally, the tissue was counterstained with hematoxylin.

H&E stain. The slides were stained with Mayer's hematoxylin (MHS, Sigma-Aldrich) and eosin (HT110, Sigma-Aldrich).

Coomassie stain. A Coomassie stain was performed for the detection of protein concentration as described in ref. [42].

Stained slides were imaged with the Nikon Ti Eclipse microscope system (Nikon) and captured using NIS 5.11.01 software (Nikon).

Clinical translation. The same imaging approach implemented in the animal study was translated for clinical scanners and human subjects, with minimal modifications as mandated by the difference in hardware and specific absorption rate (SAR) restrictions. Specifically, the continuous-wave saturation pulse was replaced by a train of off-resonant spin-lock saturation pulses (13×100 ms, 50% duty cycle[78]), and the read-out was done using gradient-echo (GRE) EPI. The MT- and amide-specific MR fingerprinting protocols (105 s each) were realized using the hardware-independent open-source pulseq framework[79] in MATLAB, with the same saturation pulse power and frequency offsets used in the preclinical study (Fig. 1b) and were played out by an interpreter on the scanner. T_1 and T_2 mapping were performed using saturation recovery (acquisition time = 68 s) and a series of five single-echo spin-echo sequences with different TE (acquisition time = 15 min), respectively. B_0 maps were acquired using the WASABI method[80] (acquisition time = 122 s). The total acquisition time was 21 min and 40 s. The research protocol was approved by the University of Tübingen Institutional Review Board and

ethics committees and the participant gave written informed consent, according to care guidelines and in compliance with the Declaration of Helsinki principles. A healthy volunteer (27-year-old male) was recruited and imaged at 3 T (Siemens Healthineers). All images had the same resolution of $1.72 \times 1.72 \times 10\,mm^3$. The decoding of the quantitative molecular information was performed similarly as the preclinical study using deep reconstruction networks trained with dictionaries simulated using the clinical acquisition protocol (Supplementary Table 1).

Image analysis. Data analysis was performed using MATLAB R2018a and Python 3.6 custom written scripts, on the basis of previously published routines as described below. T_1 and T_2 map reconstructions were performed using exponential fitting. Conventional CEST images were corrected for B_0 inhomogeneity using the WASSR method[64,81], followed by cubic spline smoothing[82,83]. The magnetization transfer ratio asymmetry (Supplementary Fig. 7a) was calculated using: $MTR_{asym} = (S^{-\Delta\omega} - S^{+\Delta\omega})/S_0$, where $S^{\pm\Delta\omega}$ is the signal measured with saturation at offset ± 3.5 ppm and S_0 is the unsaturated signal. Semi-quantitative mapping of the CEST molecular compound amplitudes was performed using a 5-pool (water, MT, amide, NOE and amine) Lorentzian fitting model (Supplementary Fig. 9d), with the starting point and boundaries described in ref. [43]. An image downsampling expedited adaptive least-squares (IDEAL) fitting approach was then implemented (Supplementary Fig. 7b–f) as described in ref. [84]. CEST MR fingerprinting with conventional dictionary matching (Supplementary Fig. 7g–l) was performed by calculating the dot product after two-norm normalization of each amide-encoded image pixel trajectory with all relevant dictionary entries (Supplementary Table 1)[44,65]. Mouse tumour ROIs (Fig. 2 and Supplementary Figs. 2, 5 and 11) were manually delineated on the basis of the T_1 and T_2 maps. The contralateral ROIs were automatically obtained by symmetrically reflecting the tumour ROIs. Suspected apoptotic ROIs were manually delineated on the basis of the decreased amide proton exchange rate. If a suspected apoptotic region existed, its area was excluded from the tumour ROI. All delineations were performed by the evaluation of a single observer blinded to the histology. ROI delineation examples are available in Fig. 2 and Supplementary Figs. 2, 5 and 11. To facilitate automatic and objective apoptotic ROI delineation, two additional approaches were also implemented (Supplementary Fig. 12): (1) A simple fixed threshold rule, where any pixel within the tumour ROI that has amide exchange rate (k_{sw}) lower than 42 Hz is considered apoptotic, and (2) a three-step segmentation on the basis of common image processing technique[85,86]. The automated segmentation method consisted of (a) automatic thresholding using Otsu's method[87] within the tumour ROI, followed by (b) finding the connected component with the largest area, and finally (c) filling remaining holes inside the component. In both delineation approaches, small noisy patches were rejected by enforcing a minimum of 30 pixels per apoptotic ROI. The above algorithms were implemented in Python using readily available functions from the open-source library scikit-image[88]. Human white matter and grey matter ROIs were automatically segmented on the basis of the T_1 map and literature T_1 values at 3 T[21], allowing a margin of 3 standard deviations from the mean.

Reporting summary. Further information on research design is available in the Nature Research Reporting Summary linked to this article.

Data availability

The main data supporting the results in this study are available within the paper and its Supplementary Information. The raw and analysed datasets generated during the study are too large to be publicly shared, but they are available for research purposes from the corresponding authors on reasonable request. Source data are provided with this paper.

Code availability

CEST MR fingerprinting dictionaries were generated on the basis of previously published methods[44,65] and used the following components: Matlab R2018a (Mathworks) and C++. These dictionaries can be reproduced using the open-source code available in https://pulseq-cest.github.io (ref. [89]) with the parameters described in Supplementary Table 1. Conventional CEST analysis can be performed using the code available in https://github.com/cest-sources. The deep-learning models can be reproduced using standard libraries and scripts available in Python 3.6 and TensorFlow 1.4.1. All source code is available from the corresponding authors upon request.

Received: 14 March 2020; Accepted: 7 July 2021;
Published online: 11 November 2021

References

1. Lichty, B. D., Breitbach, C. J., Stojdl, D. F. & Bell, J. C. Going viral with cancer immunotherapy. *Nat. Rev. Cancer* **14**, 559 (2014).
2. Markert, J. M. et al. Phase Ib trial of mutant herpes simplex virus G207 inoculated pre-and post-tumor resection for recurrent GBM. *Mol. Ther.* **17**, 199–207 (2009).
3. Tamura, K. et al. Multimechanistic tumor targeted oncolytic virus overcomes resistance in brain tumors. *Mol. Ther.* **21**, 68–77 (2013).
4. Cheema, T. A. et al. Multifaceted oncolytic virus therapy for glioblastoma in an immunocompetent cancer stem cell model. *Proc. Natl Acad. Sci. USA* **110**, 12006–12011 (2013).
5. Pol, J., Kroemer, G. & Galluzzi, L. First oncolytic virus approved for melanoma immunotherapy. *Oncoimmunlogy* **5**, e1115641 (2015).
6. Kuruppu, D. et al. Positron emission tomography of herpes simplex virus 1 oncolysis. *Cancer Res.* **67**, 3295–3300 (2007).
7. Zhou, J. et al. Differentiation between glioma and radiation necrosis using molecular magnetic resonance imaging of endogenous proteins and peptides. *Nat. Med.* **17**, 130–134 (2011).
8. Ward, K., Aletras, A. & Balaban, R. S. A new class of contrast agents for MRI based on proton chemical exchange dependent saturation transfer (CEST). *J. Magn. Reson.* **143**, 79–87 (2000).
9. van Zijl, P. C., Lam, W. W., Xu, J., Knutsson, L. & Stanisz, G. J. Magnetization transfer contrast and chemical exchange saturation transfer MRI. Features and analysis of the field-dependent saturation spectrum. *Neuroimage* **168**, 222–241 (2018).
10. Ma, D. et al. Magnetic resonance fingerprinting. *Nature* **495**, 187–192 (2013).
11. Yan, K. et al. Assessing amide proton transfer (APT) MRI contrast origins in 9L gliosarcoma in the rat brain using proteomic analysis. *Mol. Imaging Biol.* **17**, 479–487 (2015).
12. Heo, H.-Y., Zhang, Y., Lee, D.-H., Hong, X. & Zhou, J. Quantitative assessment of amide proton transfer (APT) and nuclear Overhauser enhancement (NOE) imaging with extrapolated semi-solid magnetization transfer reference (EMR) signals: application to a rat glioma model at 4.7 Tesla. *Magn. Reson. Med.* **75**, 137–149 (2016).
13. Quesson, B. et al. Magnetization transfer fast imaging of implanted glioma in the rat brain at 4.7 T: interpretation using a binary spin-bath model. *J. Magn. Reson. Imaging* **7**, 1076–1083 (1997).
14. Hobbs, S. K. et al. Magnetic resonance image–guided proteomics of human glioblastoma multiforme. *J. Magn. Reson. Imaging* **18**, 530–536 (2003).
15. Xu, J. et al. On the origins of chemical exchange saturation transfer (CEST) contrast in tumors at 9.4 T. *NMR Biomed.* **27**, 406–416 (2014).
16. Webb, B. A., Chimenti, M., Jacobson, M. P. & Barber, D. L. Dysregulated pH: a perfect storm for cancer progression. *Nat. Rev. Cancer* **11**, 671–677 (2011).
17. Jeffrey, I. W., Bushell, M., Tilleray, V. J., Morley, S. & Clemens, M. J. Inhibition of protein synthesis in apoptosis: differential requirements by the tumor necrosis factor α family and a DNA-damaging agent for caspases and the double-stranded RNA-dependent protein kinase. *Cancer Res.* **62**, 2272–2280 (2002).
18. Nilsson, C., Johansson, U., Johansson, A.-C., Kågedal, K. & Öllinger, K. Cytosolic acidification and lysosomal alkalinization during TNF-α induced apoptosis in U937 cells. *Apoptosis* **11**, 1149 (2006).
19. Hendrich, A. & Michalak, K. Lipids as a target for drugs modulating multidrug resistance of cancer cells. *Curr. Drug Targets* **4**, 23–30 (2003).
20. Gregory, R. B., Crabo, L., Percy, A. J. & Rosenberg, A. Water catalysis of peptide hydrogen isotope exchange. *Biochemistry* **22**, 910–917 (1983).
21. Stanisz, G. J. et al. T1, T2 relaxation and magnetization transfer in tissue at 3T. *Magn. Reson. Med.* **54**, 507–512 (2005).
22. Van Zijl, P. C. et al. Mechanism of magnetization transfer during on-resonance water saturation. A new approach to detect mobile proteins, peptides, and lipids. *Magn. Reson. Med.* **49**, 440–449 (2003).
23. Kettunen, M. I. & Brindle, K. M. Apoptosis detection using magnetic resonance imaging and spectroscopy. *Prog. Nucl. Magn. Reson. Spectrosc.* **3**, 175–185 (2005).
24. Kim, H. et al. Breast tumor xenografts: diffusion-weighted MR imaging to assess early therapy with novel apoptosis-inducing anti-DR5 antibody. *Radiology* **248**, 844–851 (2008).
25. Blankenberg, F. & Strauss, H. Will imaging of apoptosis play a role in clinical care? A tale of mice and men. *Apoptosis* **6**, 117–123 (2001).
26. Schellenberger, E. A. et al. Optical imaging of apoptosis as a biomarker of tumor response to chemotherapy. *Neoplasia* **5**, 187 (2003).
27. Edgington, L. E. et al. Noninvasive optical imaging of apoptosis by caspase-targeted activity-based probes. *Nat. Med.* **15**, 967 (2009).
28. Blankenberg, F. G. In vivo detection of apoptosis. *J. Nucl. Med.* **49**, 81S–95S (2008).
29. Zhao, M., Li, Z. & Bugenhagen, S. 99mTc-labeled duramycin as a novel phosphatidylethanolamine-binding molecular probe. *J. Nucl. Med.* **49**, 1345–1352 (2008).
30. Banihashemi, B. et al. Ultrasound imaging of apoptosis in tumor response: novel preclinical monitoring of photodynamic therapy effects. *Cancer Res.* **68**, 8590–8596 (2008).
31. Gallagher, F. A. et al. Magnetic resonance imaging of pH in vivo using hyperpolarized ^{13}C-labelled bicarbonate. *Nature* **453**, 940–943 (2008).
32. Blankenberg, F. G. & Norfray, J. F. Multimodality molecular imaging of apoptosis in oncology. *Am. J. Roentgen* **197**, 308–317 (2011).
33. Zhao, M., Beauregard, D. A., Loizou, L., Davletov, B. & Brindle, K. M. Non-invasive detection of apoptosis using magnetic resonance imaging and a targeted contrast agent. *Nat. Med.* **7**, 1241 (2001).

34. Zhou, J., Payen, J.-F., Wilson, D. A., Traystman, R. J. & van Zijl, P. C. Using the amide proton signals of intracellular proteins and peptides to detect pH effects in MRI. *Nat. Med.* **9**, 1085 (2003).
35. Zhao, X. et al. Saturation power dependence of amide proton transfer image contrasts in human brain tumors and strokes at 3 T. *Magn. Reson. Med.* **66**, 1033–1041 (2011).
36. Desmond, K. L. et al. Chemical exchange saturation transfer for predicting response to stereotactic radiosurgery in human brain metastasis. *Magn. Reson. Med.* **78**, 1110–1120 (2017).
37. Regnery, S. et al. Chemical exchange saturation transfer MRI serves as predictor of early progression in glioblastoma patients. *Oncotarget* **9**, 28772–28783 (2018).
38. Zaiss, M. et al. Relaxation-compensated CEST-MRI of the human brain at 7 T: unbiased insight into NOE and amide signal changes in human glioblastoma. *Neuroimage* **112**, 180–188 (2015).
39. Mehrabian, H., Myrehaug, S., Soliman, H., Sahgal, A. & Stanisz, G. J. Evaluation of glioblastoma response to therapy with chemical exchange saturation transfer. *Int. J. Radiat. Oncol. Bio. Phys.* **101**, 713–723 (2018).
40. Scheidegger, R., Wong, E. T. & Alsop, D. C. Contributors to contrast between glioma and brain tissue in chemical exchange saturation transfer sensitive imaging at 3 Tesla. *Neuroimage* **99**, 256–268 (2014).
41. Sagiyama, K. et al. In vivo chemical exchange saturation transfer imaging allows early detection of a therapeutic response in glioblastoma. *Proc. Natl Acad. Sci. USA* **111**, 4542–4547 (2014).
42. Ray, K. J. et al. Tumor pH and protein concentration contribute to the signal of amide proton transfer magnetic resonance imaging. *Cancer Res.* **79**, 1343–1352 (2019).
43. Windschuh, J. et al. Correction of B1-inhomogeneities for relaxation-compensated CEST imaging at 7 T. *NMR Biomed.* **28**, 529–537 (2015).
44. Cohen, O., Huang, S., McMahon, M. T., Rosen, M. S. & Farrar, C. T. Rapid and quantitative chemical exchange saturation transfer (CEST) imaging with magnetic resonance fingerprinting (MRF). *Magn. Reson. Med.* **80**, 2449–2463 (2018).
45. Glang, F. et al. DeepCEST 3T: robust MRI parameter determination and uncertainty quantification with neural networks — application to CEST imaging of the human brain at 3T. *Magn. Reson. Med.* **84**, 450–466 (2020).
46. Chen, L. et al. In vivo imaging of phosphocreatine with artificial neural networks. *Nat. Commun.* **11**, 1072 (2020).
47. Akbey, S., Ehses, P., Stirnberg, R., Zaiss, M. & Stöcker, T. Whole-brain snapshot CEST imaging at 7 T using 3D-EPI. *Magn. Reson. Med.* **82**, 1741–1752 (2019).
48. Setsompop, K. et al. Blipped-controlled aliasing in parallel imaging for simultaneous multislice echo planar imaging with reduced g-factor penalty. *Magn. Reson. Med.* **67**, 1210–1224 (2012).
49. Cohen, O. & Polimeni, J. R. Optimized inversion-time schedules for quantitative T1 measurements based on high-resolution multi-inversion EPI. *Magn. Reson. Med.* **79**, 2101–2112 (2018).
50. Cohen, O. & Rosen, M. S. Algorithm comparison for schedule optimization in MR fingerprinting. *Magn. Reson. Imaging* **41**, 15–21 (2017).
51. Sommer, K. et al. Towards predicting the encoding capability of MR fingerprinting sequences. *Magn. Reson. Imaging* **41**, 7–14 (2017).
52. Zhu, B., Liu, J., Koonjoo, N., Rosen, B. & Rosen, M. S. Automated pulse sequence generation (Autoseq) and neural network decoding for fast quantitative MR parameter measurement using continuous and simultaneous RF transmit and receive. In *ISMRM 27th Annual Meeting & Exhibition* (ISMRM, 2019).
53. Guicciardi, M. E., Malhi, H., Mott, J. L. & Gores, G. J. Apoptosis and necrosis in the liver. *Compr. Physiol.* **3**, 977–1010 (2013).
54. Borys, J. et al. Free radical production, inflammation and apoptosis in patients treated with titanium mandibular fixations—an observational study. *Front. Immunol.* **10**, 2662 (2019).
55. Radi, E., Formichi, P., Battisti, C. & Federico, A. Apoptosis and oxidative stress in neurodegenerative diseases. *J. Alzheimers Dis.* **42**, S125–S152 (2014).
56. Zhou, J., Heo, H.-Y., Knutsson, L., van Zijl, P. C. & Jiang, S. APT-weighted MRI: techniques, current neuro applications, and challenging issues. *J. Magn. Reson. Imaging* **50**, 347–364 (2019).
57. Sakata, A. et al. Grading glial tumors with amide proton transfer MR imaging: different analytical approaches. *J. Neurooncol.* **122**, 339–348 (2015).
58. Gilad, A. A. et al. Artificial reporter gene providing MRI contrast based on proton exchange. *Nat. Biotechnol.* **25**, 217–219 (2007).
59. Farrar, C. T. et al. Establishing the lysine-rich protein CEST reporter gene as a CEST MR imaging detector for oncolytic virotherapy. *Radiology* **275**, 746–754 (2015).
60. Meier, S. et al. Non-invasive detection of adeno-associated viral gene transfer using a genetically encoded CEST-MRI reporter gene in the murine heart. *Sci. Rep.* **8**, 4638 (2018).
61. Mehrabian, H., Desmond, K. L., Soliman, H., Sahgal, A. & Stanisz, G. J. Differentiation between radiation necrosis and tumor progression using chemical exchange saturation transfer. *Clin. Cancer Res.* **23**, 3667–3675 (2017).
62. Henkelman, R., Stanisz, G. & Graham, S. Magnetization transfer in MRI: a review. *NMR Biomed.* **14**, 57–64 (2001).
63. Wang, R. et al. Amide proton transfer magnetic resonance imaging of Alzheimer's disease at 3.0 Tesla: a preliminary study. *Chin. Med. J.* **128**, 615 (2015).
64. Kim, M., Gillen, J., Landman, B. A., Zhou, J. & van Zijl, P. C. Water saturation shift referencing (WASSR) for chemical exchange saturation transfer (CEST) experiments. *Magn. Reson. Med.* **61**, 1441–1450 (2009).
65. Perlman, O. et al. CEST MR-fingerprinting: practical considerations and insights for acquisition schedule design and improved reconstruction. *Magn. Reson. Med.* **83**, 462–478 (2020).
66. Cohen, O., Zhu, B. & Rosen, M. S. MR fingerprinting deep reconstruction network (DRONE). *Magn. Reson. Med.* **80**, 885–894 (2018).
67. Balsiger, F. et al. Magnetic resonance fingerprinting reconstruction via spatiotemporal convolutional neural networks. In *International Workshop on Machine Learning for Medical Image Reconstruction* (Springer, 2018).
68. Kingma, D. P. & Ba, J. Adam: a method for stochastic optimization. Preprint at https://arxiv.org/abs/1412.6980 (2014).
69. Zur, R. M., Jiang, Y., Pesce, L. L. & Drukker, K. Noise injection for training artificial neural networks: a comparison with weight decay and early stopping. *Med. Phys.* **36**, 4810–4818 (2009).
70. Nakashima, H. et al. Toxicity and efficacy of a novel GADD34-expressing oncolytic HSV-1 for the treatment of experimental glioblastoma. *Clin. Cancer Res.* **24**, 2574–2584 (2018).
71. McMahon, M. T. et al. Quantifying exchange rates in chemical exchange saturation transfer agents using the saturation time and saturation power dependencies of the magnetization transfer effect on the magnetic resonance imaging signal (QUEST and QUESP): pH calibration for poly-l-lysine and a starburst dendrimer. *Magn. Reson. Med.* **55**, 836–847 (2006).
72. Longo, D. L. et al. In vitro and in vivo assessment of non-ionic iodinated radiographic molecules as chemical exchange saturation transfer magnetic resonance imaging tumor perfusion agents. *Invest. Radiol.* **51**, 155–162 (2016).
73. Goldenberg, J. M. & Pagel, M. D. Assessments of tumor metabolism with CEST MRI. *NMR Biomed.* **32**, e3943 (2019).
74. Anemone, A., Consolino, L. & Longo, D. L. MRI-CEST assessment of tumour perfusion using x-ray iodinated agents: comparison with a conventional Gd-based agent. *Eur. Radiol.* **27**, 2170–2179 (2017).
75. High, R. A. et al. In vivo assessment of extracellular pH of joint tissues using acidoCEST-UTE MRI. *Quant. Imaging Med. Surg.* **9**, 1664 (2019).
76. Virtanen, P. et al. Scipy 1.0: fundamental algorithms for scientific computing in python. *Nat. Methods* **17**, 261–272 (2020).
77. Kumari, N., Thakur, N., Cho, H. R. & Choi, S. H. Assessment of early therapeutic response to nitroxoline in temozolomide-resistant glioblastoma by amide proton transfer imaging: a preliminary comparative study with diffusion-weighted imaging. *Sci. Rep.* **9**, 5585 (2019).
78. Roeloffs, V., Meyer, C., Bachert, P. & Zaiss, M. Towards quantification of pulsed spinlock and CEST at clinical MR scanners: an analytical interleaved saturation–relaxation (ISAR) approach. *NMR Biomed.* **28**, 40–53 (2015).
79. Layton, K. J. et al. Pulseq: a rapid and hardware-independent pulse sequence prototyping framework. *Magn. Reson. Med.* **77**, 1544–1552 (2017).
80. Schuenke, P. et al. Simultaneous mapping of water shift and B1 (WASABI) – application to field – inhomogeneity correction of CEST MRI data. *Magn. Reson. Med.* **77**, 571–580 (2017).
81. Liu, G., Gilad, A. A., Bulte, J. W., van Zijl, P. C. & McMahon, M. T. High-throughput screening of chemical exchange saturation transfer MR contrast agents. *Contrast Media Mol. Imaging* **5**, 162–170 (2010).
82. Chen, L. Q. et al. Evaluations of extracellular pH within in vivo tumors using acidoCEST MRI. *Magn. Reson. Med.* **72**, 1408–1417 (2014).
83. Stancanello, J. et al. Development and validation of a smoothing-splines-based correction method for improving the analysis of CEST-MR images. *Contrast Media Mol. Imaging* **3**, 136–149 (2008).
84. Zhou, I. Y. et al. Quantitative chemical exchange saturation transfer (CEST) MRI of glioma using image downsampling expedited adaptive least-squares (IDEAL) fitting. *Sci. Rep.* **7**, 84 (2017).
85. Banerjee, S., Mitra, S. & Shankar, B. U. Single seed delineation of brain tumor using multi-thresholding. *Inf. Sci.* **330**, 88–103 (2016).
86. Gordillo, N., Montseny, E. & Sobrevilla, P. State of the art survey on MRI brain tumor segmentation. *Magn. Reson. Imaging* **31**, 1426–1438 (2013).
87. Otsu, N. A threshold selection method from gray-level histograms. *IEEE Trans. Syst. Man Cybern.* **9**, 62–66 (1979).
88. van der Walt, S. et al. scikit-image: image processing in python. *PeerJ* **2**, e453 (2014).
89. Herz, K. et al. Pulseq-CEST: towards multi-site multi-vendor compatibility and reproducibility of CEST experiments using an open-source sequence standard. *Magn. Reson. Med.* **86**,1845–1858 (2021).
90. Zaiß, M., Schmitt, B. & Bachert, P. Quantitative separation of CEST effect from magnetization transfer and spillover effects by Lorentzian-line-fit analysis of Z-spectra. *J. Magn. Reson.* **211**, 149–155 (2011).

91. Geades, N. et al. Quantitative analysis of the Z-spectrum using a numerically simulated look-up table: application to the healthy human brain at 7T. *Magn. Reson. Med.* **78**, 645–655 (2017).
92. Liu, D. et al. Quantitative characterization of nuclear Overhauser enhancement and amide proton transfer effects in the human brain at 7 Tesla. *Magn. Reson. Med.* **70**, 1070–1081 (2013).
93. Yarnykh, V. L. et al. Fast whole-brain three-dimensional macromolecular proton fraction mapping in multiple sclerosis. *Radiology* **274**, 210–220 (2015).
94. Samsonov, A. et al. Quantitative MR imaging of two-pool magnetization transfer model parameters in myelin mutant shaking pup. *Neuroimage* **62**, 1390–1398 (2012).
95. Heo, H.-Y. et al. Quantifying amide proton exchange rate and concentration in chemical exchange saturation transfer imaging of the human brain. *Neuroimage* **189**, 202–213 (2019).

Acknowledgements

The work was supported by the US National Institutes of Health Grants R01-CA203873 (C.T.F.), P41-RR14075 (Massachusetts General Hospital), S10-RR023401 (Massachusetts General Hospital), S10-RR019307 (Massachusetts General Hospital) and 1S10RR023043 (Massachusetts General Hospital), as well as by R01-NS110942 (H.N., E.A.C.) and P01-CA163205 (H.N., E.A.C.). The Brigham and Women's Small Animal Imaging Laboratory (SAIL) was funded by a G20 Grant (G20-RR031051) as part of the American Recovery and Reinvestment Act as part of the construction of the Brigham and Women's MRI Research Center (BWMRC). The 7T Bruker Small Bore Animal Magnet was partially funded by an S10 Grant (S10-OD010705) through the National Institutes of Health. K.H was supported by the German Research Foundation (DFG, grant ZA 814/2–1). This project also received funding from the European Union's Horizon 2020 research and innovation programme under the Marie Skłodowska-Curie grant agreement No. 836752 (OncoViroMRI). This paper reflects only the authors' view, and the Research Executive Agency of the European Commission is not responsible for any use that may be made of the information it contains.

Author contributions

O.P., O.C., M.S.R. and C.T.F. conceptualized the deep-learning reconstruction architecture. O.P., K.H., M.Z., O.C. and C.T.F. implemented and tested various aspects of the technical framework. H.I., H.N., E.A.C., O.P. and C.T.F. contributed to preclinical experiment design. H.I. performed tumour implantations and virus inoculations. O.P., C.T.F. and H.I. performed the preclinical imaging. N.S. performed the histology and immunohistochemistry studies. K.H., M.Z., O.P. and C.T.F. developed the clinical imaging scheme. K.H. and M.Z. performed the clinical imaging. O.P., H.I., K.H., N.S., H.N., M.Z., E.A.C., O.C., M.S.R. and C.T.F. wrote and/or substantially revised the manuscript.

Competing interests

The authors declare the following competing interests: C.T.F., M.S.R. and O.C. hold a patent for the CEST MR fingerprinting method (patent no. US10,605,877).

Additional information

Supplementary information The online version contains supplementary material available at https://doi.org/10.1038/s41551-021-00809-7.

Correspondence and requests for materials should be addressed to Or Perlman or Christian T. Farrar.

Peer review information *Nature Biomedical Engineering* thanks the anonymous reviewer(s) for their contribution to the peer review of this work. Peer reviewer reports are available.

Reprints and permissions information is available at www.nature.com/reprints.

Publisher's note Springer Nature remains neutral with regard to jurisdictional claims in published maps and institutional affiliations.

nature research

Corresponding author(s): Or Perlman and Christian T. Farrar

Last updated by author(s): Jun 19, 2021

Reporting Summary

Nature Research wishes to improve the reproducibility of the work that we publish. This form provides structure for consistency and transparency in reporting. For further information on Nature Research policies, see our Editorial Policies and the Editorial Policy Checklist.

Statistics

For all statistical analyses, confirm that the following items are present in the figure legend, table legend, main text, or Methods section.

n/a	Confirmed	
☐	☒	The exact sample size (*n*) for each experimental group/condition, given as a discrete number and unit of measurement
☐	☒	A statement on whether measurements were taken from distinct samples or whether the same sample was measured repeatedly
☐	☒	The statistical test(s) used AND whether they are one- or two-sided *Only common tests should be described solely by name; describe more complex techniques in the Methods section.*
☐	☒	A description of all covariates tested
☐	☒	A description of any assumptions or corrections, such as tests of normality and adjustment for multiple comparisons
☐	☒	A full description of the statistical parameters including central tendency (e.g. means) or other basic estimates (e.g. regression coefficient) AND variation (e.g. standard deviation) or associated estimates of uncertainty (e.g. confidence intervals)
☐	☒	For null hypothesis testing, the test statistic (e.g. *F*, *t*, *r*) with confidence intervals, effect sizes, degrees of freedom and *P* value noted *Give P values as exact values whenever suitable.*
☒	☐	For Bayesian analysis, information on the choice of priors and Markov chain Monte Carlo settings
☒	☐	For hierarchical and complex designs, identification of the appropriate level for tests and full reporting of outcomes
☐	☒	Estimates of effect sizes (e.g. Cohen's *d*, Pearson's *r*), indicating how they were calculated

Our web collection on statistics for biologists contains articles on many of the points above.

Software and code

Policy information about availability of computer code

Data collection	Animal MRI data were collected using Bruker Paravision software (version 6) installed on a 7T Bruker scanner (Bruker Biospin, Ettlingen, Germany). Human MRI data were collected using a Siemens Healthineers Prisma 3T scanner, and a pulse sequence implemented using the open source pulseq software version 1.3.0 (https://pulseq.github.io/). Stained slides were captured by NIS 5.11.01 software (Nikon, Minato-ku, Japan).
Data analysis	CEST MR-fingerprinting dictionaries were generated on the basis of previously published methods (refs. 44, 65) and the use of the following components: Matlab R2018a (Mathworks, Natick, MA, USA) and C++. These dictionaries can be reproduced using the open-source code available at https://pulseq-cest.github.io (ref. 89), with the parameters described in Supplementary Table 1. Conventional CEST analysis can be performed using the code available at https://www.cest-sources.org. (ref. 90). The deep-learning models can be reproduced using standard libraries and scripts available in Python 3.6 and TensorFlow 1.4.1. All source code is available from the corresponding authors on request.

For manuscripts utilizing custom algorithms or software that are central to the research but not yet described in published literature, software must be made available to editors and reviewers. We strongly encourage code deposition in a community repository (e.g. GitHub). See the Nature Research guidelines for submitting code & software for further information.

Data

Policy information about availability of data

All manuscripts must include a data availability statement. This statement should provide the following information, where applicable:

- Accession codes, unique identifiers, or web links for publicly available datasets
- A list of figures that have associated raw data
- A description of any restrictions on data availability

The main data supporting the results in this study are available within the paper and its Supplementary Information. The raw and analysed datasets generated during the study are too large to be publicly shared, yet they are available for research purposes from the corresponding authors on reasonable request.

Field-specific reporting

Please select the one below that is the best fit for your research. If you are not sure, read the appropriate sections before making your selection.

☒ Life sciences ☐ Behavioural & social sciences ☐ Ecological, evolutionary & environmental sciences

For a reference copy of the document with all sections, see nature.com/documents/nr-reporting-summary-flat.pdf

Life sciences study design

All studies must disclose on these points even when the disclosure is negative.

Sample size	On the basis of our previous studies in mice, we assumed MRI-signal changes in amide proton exchange rate (ksw) of 4 Hz, a standard deviation of 1.5 Hz, a statistical power of 80%, and a 5% significance level. The calculation resulted in 8 mice. Given our previous experience with the mortality associated with this animal model, 4 additional animals were used. For the single-human healthy-volunteer imaging experiment, the goal was to show translational potential at the proof-of-concept level; therefore, no sample-size calculation was required or performed.
Data exclusions	The following two pre-established exclusion criteria were imposed: unsuccessful tumour implantation (occurred in 1 mouse out of 16); corrupted image data (occurred in 2 image sets out of 39, potentially owing to RF coil or transmitter error).
Replication	At least 3 replications were independently performed, and the attempts at replications were successful.
Randomization	All mice were randomly allocated into groups. For the human study, randomization was not relevant, as only a single human healthy volunteer was imaged.
Blinding	After MRI acquisition, the collected data were first blinded and then processed. MRI acquisition and tissue histology processing were performed by different individuals. The MR-image processing was performed by a person blinded to the histology. In all other experiments, the investigators were blinded to group allocation during data collection and analysis.

Reporting for specific materials, systems and methods

We require information from authors about some types of materials, experimental systems and methods used in many studies. Here, indicate whether each material, system or method listed is relevant to your study. If you are not sure if a list item applies to your research, read the appropriate section before selecting a response.

Materials & experimental systems

n/a	Involved in the study
☐	☒ Antibodies
☒	☐ Eukaryotic cell lines
☒	☐ Palaeontology and archaeology
☐	☒ Animals and other organisms
☐	☒ Human research participants
☒	☐ Clinical data
☒	☐ Dual use research of concern

Methods

n/a	Involved in the study
☒	☐ ChIP-seq
☒	☐ Flow cytometry
☐	☒ MRI-based neuroimaging

Antibodies

Antibodies used	Primary antibodies against HSV 1 (B0114, Dako); caspase 3 (9579, Cell Signaling Technology); Ki-67 (MA5-14520, Invitrogen)
Validation	HSV-1 staining was validated as an immunohistochemistry assay using anti-HSV-1 polyclonal antibody (DAKO B0114) on formalin-fixed, paraffine-embedded (FFPE) tissues of athymic mouse brains implanted with U87dEGFR, subject to the HSV-1 injection as positive sample and PBS injection as negative sample.

Other antibodies for cleaved caspase 3 and Ki-67 were obtained from commercial sources and validated for each application by the manufacturers. They have been highly cited, and validated by multiple labs. According to the manufacturers' websites:

- Antibodies for cleaved caspase 3 (9579, Cell Signaling Technology) have been cited in 135 publications, including the following reference, where rabbit polyclonal anti-Cleaved caspase 3 antibodies were validated for immunohistochemistry using mouse paraffin tissue sections: Riopel M. et al. J. Clin. Invest. 128, 1458–1470 (2018).

- Antibodies for Ki-67 (MA5-14520, Invitrogen) have been cited in 643 publications, including Finkin, Shlomi, et al. "Ectopic lymphoid structures function as microniches for tumor progenitor cells in hepatocellular carcinoma" Nat. Immunol. 16, 1235–1244 (2015). This Antibody was verified by the manufacturer using cell treatment to ensure that the antibody binds to the antigen stated as detailed in: https://www.thermofisher.com/antibody/product/Ki-67-Antibody-clone-SP6-Recombinant-Monoclonal/MA5-14520

Animals and other organisms

Policy information about studies involving animals; ARRIVE guidelines recommended for reporting animal research

Laboratory animals	Sixteen 6-to-8-week-old female athymic mice (BALB/c, nu/nu) and a single 6-to-8-week-old female C57/BL6 mouse were purchased from Envigo. The mice weighed 19–23 g.
Wild animals	The study did not involve wild animals.
Field-collected samples	The study did not involve samples collected from the field.
Ethics oversight	All experimental protocols were approved by the Institutional Animal Care and Use Committees (IACUC) of the Brigham and Women's Hospital. All animal experiments were carried out in accordance with approved IACUC ethical guidelines and regulations.

Note that full information on the approval of the study protocol must also be provided in the manuscript.

Human research participants

Policy information about studies involving human research participants

Population characteristics	One healthy, 27-year-old male.
Recruitment	A co-worker from a different research group volunteered for the study. No bias is expected to affect the results, as no functional imaging was performed and only objective chemical-exchange brain parameters were automatically quantified.
Ethics oversight	The research protocol was approved by the University of Tübingen IRB and ethics committees, and the participant gave written informed consent, according to CARE guidelines and in compliance with the Declaration of Helsinki principles.

Note that full information on the approval of the study protocol must also be provided in the manuscript.

Magnetic resonance imaging

Experimental design

Design type	The quantification of magnetic tissue properties was performed by using established T1, T2 and field homogeneity (B0) protocols. Chemical exchange saturation transfer (CEST) parameters were encoded and imaged using the proposed MR-fingerprinting approach. Conventional CEST imaging was performed for comparison. No functional imaging was performed.
Design specifications	In animals, Imaging was performed at 8–11 days after brain-tumor implantation. Next, a herpes-simplex-virus-type-I-derived oncolytic virus, NG34, was inoculated intratumourally in 12 mice (the other 4 served as control), and the imaging was repeated 48 and 72 h later. For the healthy human subject, a single volunteer was imaged in a single imaging session.
Behavioral performance measures	Not applicable, as no fMRI or behavioral experiments were conducted.

Acquisition

Imaging type(s)	Structural (using T1/T2/B0) and Chemical Exchange Saturation Transfer (CEST) scans.
Field strength	For the animal study: 7T; for the human study: 3T; for the phantom study 4.7T and 9.4T.
Sequence & imaging parameters	Animal study: Two chemical exchange saturation transfer (CEST) MR-fingerprinting acquisition protocols were employed sequentially (105s each, Fig. 1a-b), designed for encoding the semi-solid macromolecule (denoted as MT, magnetization transfer) and amide information into unique trajectories. The first protocol was aimed for magnetic labeling the MT pool, varying the saturation pulse frequency offset between 6-14 ppm (to avoid amide/amine/aliphatic nuclear Overhauser effect (NOE) contributions) and the saturation pulse power between 0–4 μT. The second protocol was aimed for magnetic labeling the amide pool (in the presence of MT), using the same saturation pulse power schedule but with a fixed saturation pulse frequency offset at 3.5 ppm. Both protocols had repetition-time/echo-time (TR/TE) = 3500/20 ms, a

flip angle of 90°, a continuous saturation pulse of 2500 ms, and a spin-echo echo-planar-imaging (SE-EPI) readout. T1 maps were acquired using the variable repetition-time rapid acquisition with relaxation enhancement (RARE) protocol, with TR = 200, 400, 800, 1500, 3000, and 5500 ms, TE = 7 ms, RARE factor = 2. T2 maps were acquired using the multi-echo spin-echo protocol, TR = 2000 ms, 25 TE values between 8-200 ms. Static magnetic field B0 maps were acquired using the water saturation shift referencing (WASSR) protocol, employing a saturation pulse power of 0.3 µT, TR/TE = 8000/20 ms, flip-angle = 90°, saturation duration = 3000 ms, and a saturation pulse frequency varying between -1 to 1 ppm in 0.1 ppm increments. A traditional full Z-spectrum CEST scan was performed for comparison, using a SE-EPI sequence with TR/TE = 8000/20 ms, flip-angle = 90°, and pre-saturation pulses of 0.7 µT and 3000 ms, at –7 to 7 ppm frequency offsets with 0.25 ppm increments and a no-saturation reference image. The field of view (19 mm x 19 mm x 1 mm) and image resolution (297 x 297 x 1000 µm3) were identical for all scans besides a high-resolution (148 x 148 x 1000 µm3) T2-weighted scan (TR/TE = 2000/60 ms), taken as reference.

Human study:
The same imaging approach implemented in the animal study was translated for clinical scanners and human subjects, with minimal modifications, as mandated by the difference in hardware and specific absorption rate (SAR) restrictions. Specifically, the continuous-wave saturation pulse was replaced by a train of off-resonant spin-lock saturation pulses (13 x 100 ms, 50% duty-cycle), and the read-out was done using gradient-echo (GRE) EPI. The MT and amide specific MR-fingerprinting protocols were realized using the hardware-independent open-source pulseq framework (ref. 55) in MATLAB, with the same saturation pulse power and frequency offsets used in the preclinical study (Fig. 1b), and were played out by an interpreter on the scanner. T1 and T2 mapping were performed using saturation recovery and a series of five single-echo spin-echo sequences with different TE, respectively. B0 maps were acquired using the WASABI method (ref. 56). All images had the same resolution of 1.72 x 1.72 x 10 mm3.

Area of acquisition

Brain-tumor-bearing animals: a whole brain T2-weighted scan was used to find the tumour location. All other protocols used a single slice with a fixed geometry (297 x 297 x 1000 µm3), centered on the tumour center.

Human: a single slice (1.72 x 1.72 x 10 mm3) was imaged based on the default iso-center coordinates defined in pulseq software.

Diffusion MRI ☐ Used ☒ Not used

Preprocessing

Preprocessing software

Data analysis was performed using MATLAB R2018a and Python 3.6 custom-written scripts, based on previously published routines.

Normalization

Conventional CEST images were corrected for B0 in-homogeneity using the WASSR method and normalized using a reference no-saturation image. Conventional raw CEST MR-fingerprinting images were 2-norm normalized along the temporal axis. AI-boosted CEST MR-fingerprinting raw trajectories were normalized to zero mean and unit standard deviation along the temporal axis.

Normalization template

Not applicable, as no regional functional MRI analysis was carried out or required. Tumour regions were not bounded to a particular brain region and thus no atlas and normalization template were required. For the human study, a single volunteer was imaged using a single image slice, and thus no normalization template was required. Human white matter and gray matter ROIs were automatically segmented on the basis of the T1-map and on literature T1 values at 3T (ref. 21), allowing a margin of three standard deviations from the mean.

Noise and artifact removal

CEST Z-spectra were cubic spline smoothed, as performed in refs 82, 83.

Volume censoring

Not applicable, as no fMRI/diffusion studies were performed. No censoring was performed and no severe motion occurred during the MRI scans.

Statistical modeling & inference

Model type and settings

Not applicable, as no functional imaging was performed.

Effect(s) tested

Not applicable, as no functional imaging was performed.

Specify type of analysis: ☐ Whole brain ☐ ROI-based ☒ Both

Anatomical location(s)

Mouse tumor regions of interest (ROIs) (Fig. 2; Extended Data Fig. 1) were manually delineated on the basis of the T1 and T2 maps. The contralateral ROIs were automatically obtained by symmetrically reflecting the tumour ROIs. Suspected apoptotic ROIs were delineated on the basis of decreased amide proton exchange rate.

Anatomical location(s). If a suspected apoptotic region existed, its area was excluded from the tumor ROI. All delineations were performed by a single observer blinded to the histology. Human white matter and gray matter ROIs were automatically segmented on the basis of the T1-map and on literature T1 values at 3T, allowing a margin of three standard deviations from the mean.

Statistic type for inference (See Eklund et al. 2016)

Not applicable, as no functional imaging was performed.

Correction

Not applicable, as no functional imaging was performed.

Models & analysis

n/a	Involved in the study
☒	☐ Functional and/or effective connectivity
☒	☐ Graph analysis
☒	☐ Multivariate modeling or predictive analysis